PCCP

PAPER

View Article Online
View Journal | View Issue

Cite this: *Phys. Chem. Chem. Phys.*, 2015, **17**, 17288

Li^+ intercalation in isostructural Li_2VO_3 and Li_2VO_2F with O^{2-} and mixed O^{2-}/F^- anions†

Ruiyong Chen,*[ab] Shuhua Ren,[b] Murat Yavuz,[acd] Alexander A. Guda,[e] Viktor Shapovalov,[e] Raiker Witter,[bf] Maximilian Fichtner[ab] and Horst Hahn[abg]

Received 29th April 2015,
Accepted 8th June 2015

DOI: 10.1039/c5cp02505b

www.rsc.org/pccp

Mixed-anion materials for Li-ion batteries have been attracting attention in view of their tunable electrochemical properties. Herein, we compare two isostructural ($Fm\bar{3}m$) model intercalation materials Li_2VO_3 and Li_2VO_2F with O^{2-} and mixed O^{2-}/F^- anions, respectively. Synchrotron X-ray diffraction and pair distribution function data confirm large structural similarity over long-range and at the atomic scale for these materials. However, they show distinct electrochemical properties and kinetic behaviour arising from the different anion environments and the consequent difference in cationic electrostatic repulsion. In comparison with Li_2VO_3 with an active $V^{4+/5+}$ redox reaction, the material Li_2VO_2F with oxofluoro anions and the partial activity of $V^{3+/5+}$ redox reaction favor higher theoretical capacity (460 mA h g^{-1} *vs.* 230 mA h g^{-1}), higher voltage (2.5 V *vs.* 2.2 V), lower polarization (0.1 V *vs.* 0.3 V) and faster Li^+ chemical diffusion ($\sim 10^{-9}$ cm^2 s^{-1} *vs.* $\sim 10^{-11}$ cm^2 s^{-1}). This work not only provides insights into the understanding of anion chemistry, but also suggests the rational design of new mixed-anion battery materials.

1. Introduction

Rechargeable Li-ion batteries are among the most desired choices for future electrochemical energy storage.[1,2] The performance of Li-ion batteries is governed by the crystal structure and the active element(s) of the electrode materials. Understanding the role of anions, which acts as pillars for the crystal framework, is of importance for advancing the performance of electrode materials. Transition metal oxides (MO_x)[3] and lithium transition metal oxides (Li–M–O)[4–7] with O^{2-} anions have demonstrated pronounced variation as the materials to be used or considered. The metal–ligand bonding character (ionic/covalent) and the bond strength are crucial factors to determine the redox potentials[8] and the Li^+ storage mechanism (intercalation/conversion).[9] The incorporation of guest anions of high electronegativity into the crystal lattice is found to be an effective strategy to enhance the electrode performance.[10,11] Mixed-anion materials have become a new avenue for developing promising candidates with versatile crystal chemistry and physicochemical properties.[12–15] However, the parent crystal symmetry is often altered by introducing guest anions, making it difficult to identify the individual function of anions governing the performance. Anion partitioning is often observed in mixed-anion materials upon lithiation (such as FeOF, with the formation of separate oxide and fluoride phases) in the case of large mismatch in the bonding between metal and different anion ligands.[13,16] This leads to a conversion reaction at low voltage plateaus and the initial active phase can hardly be recovered.[16] In contrast, early transition metal compounds with strong metal-ligand bonding (such as vanadium-based oxides and vanadates) are favourable for Li^+ intercalation reaction without metal–oxygen bond cleavage.[17] So far, candidate compounds of vanadium-based mixed anion materials for Li-ion batteries are extremely rare. We have previously reported a new oxyfluoride intercalation compound Li_2VO_2F,[18] which has a high theoretical capacity of about 462 mA h g^{-1} and a stable crystal structure for more than one-electron reactions. It outperforms any known vanadium oxide and vanadate with respect to reversible capacity and structural stability.[17] The realization of high capacity intercalation compounds based on mixed-anion oxyfluoride is of great importance. Identifying the fundamental aspects related to a number of material properties requires detailed knowledge of how the intermixed O^{2-}/F^- anion environment affects the structural features and the kinetic quantities.

[a] *Helmholtz Institute Ulm for Electrochemical Energy Storage, 89081 Ulm, Germany. E-mail: ruiyong.chen@kit.edu, hc18chen@gmail.com*
[b] *Institute of Nanotechnology, Karlsruhe Institute of Technology, P.O. Box 3640, 76021 Karlsruhe, Germany*
[c] *Institute for Applied Materials, Karlsruhe Institute of Technology, P.O. Box 3640, 76021 Karlsruhe, Germany*
[d] *Materials Science, Technische Universität Darmstadt, 64287 Darmstadt, Germany*
[e] *International Research Center–Smart Materials, Southern Federal University, 344090 Rostov-on-Don, Russia*
[f] *Technomedicum, Tallinn University of Technology, 19086 Tallinn, Estonia*
[g] *Joint Research Laboratory Nanomaterials, Institute of Materials Science, Technische Universität Darmstadt, 64287 Darmstadt, Germany*

† Electronic supplementary information (ESI) available: Rietveld refinement, PDF, Raman, NMR, EPR and EIS data. See DOI: 10.1039/c5cp02505b

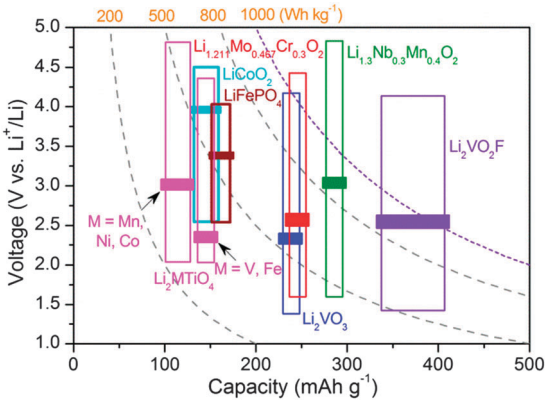

Fig. 1 Typical operating voltage/capacity range/energy density plots for various reported DRS (space group $Fm\bar{3}m$) cathode materials of Li-ion batteries.[18–24] The bars indicate the average voltages. $LiFePO_4$ and $LiCoO_2$ are also shown for comparison.

The Li^+ storage hosts based on oxides with disordered rocksalt (DRS) structure (space group $Fm\bar{3}m$, No. 225) have received renewed interest because of their capability to extend the reversible capacity compared to classic cathode materials, stable phase for Li^+ intercalation storage and a low lattice volume change for Li^+ uptake/removal.[19–24] To date, several such cation-DRS materials with a typical formula of $Li_{1.211}Mo_{0.467}Cr_{0.3}O_2$,[19] $Li_{1.3}Nb_{0.3}Mn_{0.4}O_2$,[20] $Li_{1.2}Ni_{0.4}Ti_{0.4}O_2$[21] and Li_2MTiO_4[22–24] have been reported, as summarized in Fig. 1. These Li-rich materials show an average operating voltage of about 2.2–3.1 V. All Li^+ and metal cations are distributed randomly at the crystallographically equivalent site (4*a* Wyckoff site) in the DRS structure. The anionic sublattice (4*b* Wyckoff site) is exclusively occupied by close-packed oxygen. Note that the stoichiometric $LiMO_2$ with DRS showed negligible Li^+ storage activity[25] due to the high energy barrier for Li^+ diffusion.[19,26] The structure-Li^+ mobility relationships for such a class of materials have recently been clarified by Ceder *et al.*[26] The Li-rich composition creates macroscopic percolation pathways spanning the entire DRS structure for Li^+ diffusion. However, experimental observations elucidating the dependence of Li^+ diffusion on the anion environment in isostructural compounds are still lacking. Compared to reported cation-DRS materials with only mono O^{2-} anions,[19–24] the material with mixed anions provides a wide variety to develop new disordered electrode materials with enhanced performance.

To access the importance of the anion chemistry and to correlate the chemical features of materials to their electrochemical properties, we herein perform a direct experimental comparison between two isostructural model intercalation compounds Li_2VO_3 and Li_2VO_2F with oxo and oxofluoro anions, respectively. We show how F^- anion incorporation can affect positively the key electrochemical properties in terms of capacity, voltage, hysteresis, charge transfer resistance and Li^+ transport, without alternating the DRS crystal structure. These insights into anion chemistry in disordered materials are suggestive for tuning the material properties and therefore open up new possibilities for energy storage materials based on the DRS structure with a rational design of the anionic sublattice.

2. Experimental

2.1. Synthesis

All materials were synthesized by a ball-milling route (Retsch PM100, WC jar and balls) in an argon atmosphere. For Li_2VO_2F, the precursors of Li_2O, LiF and V_2O_3 were used (450 rpm, 40 h). For Li_2VO_3, the precursors of Li_2O and V_2O_4 were used (400 rpm, 14 h). The starting materials were mixed with intended stoichiometric amounts together with an excess of 10 wt% Li_2O to compensate for lithium loss during synthesis.

2.2. Electrochemical studies

For electrochemical performance tests, the as-obtained materials were ball-milled with Super P carbon (20 wt%) at 300 rpm for 10 h. A slurry was fabricated by mixing the active powder (72 wt%)/Super P (18 wt%) composite and 10 wt% poly(vinylidene fluoride-hexafluoropropylene) (Solef 5130) in dimethylformamide (DMF). The slurry was coated on a stainless steel current collector and dried under vacuum at 90 °C. The loading of the active material on the current collector was about 3 mg cm^{-2}. The electrochemical charge–discharge performance was evaluated with lithium as the anode and $LiPF_6$ (1 M in ethylene carbonate and dimethyl carbonate, 1 : 1 volume ratio) as electrolyte using a Swagelok cell in the same voltage range of 1.3–4.1 V at 25 °C. For *ex situ* structural characterization, samples were collected after disassembling the cell and washed with dimethyl carbonate. Electrochemical impedance spectroscopy (EIS) measurements were performed at 25 °C using a Bio-Logic instrument in the frequency range of 100 kHz–1 mHz with an AC voltage of 5 mV. Prior to EIS measurements, the cathode materials were cycled to the requested voltages and then held for 2 h to reach a quasi-equilibrium state.

2.3. Synchrotron XRD and PDF analysis

Synchrotron X-ray diffraction (XRD) data were collected at beamline BL04, MSPD (λ = 0.41343 Å) at the ALBA Synchrotron Light Source, Spain. The powders were loaded into 0.7 mm glass capillaries in an argon-filled glovebox. The high energy X-rays were used to access the high magnitude of scattering vectors of Q_{max} = 26 $Å^{-1}$ ($Q = 4\pi \sin\theta/\lambda$) for the success of atomic pair distribution function (PDF) analysis. The scattered radiation was collected using a Mythen II detector. The diffraction patterns were refined using the Rietveld method using the FullProf program.[27] The PDF, $G(r)$, provides the probability of finding atomic pairs separated by the real space distance (r) in a sample, weighted by the concentration and scattering power of the contributing atoms. Raw X-ray total scattering data were processed using the program Fit2D[28] and then Fourier transformed to yield the PDF, $G(r)$, using PDFgetX3.[29] PDFFIT[30] was used to refine the structural models.

2.4. V K-Edge XANES

The vanadium K-edge X-ray absorption near edge structure (XANES) spectra was recorded using an in-house Rigaku R-XAS spectrometer in transmission mode at room temperature with a crystal monochromator Ge(311) and an energy resolution of 0.7 eV,

at the Southern Federal University, Russia. Pellets were prepared in a glovebox and sealed in an X-ray transparent plastic bag in an inert atmosphere. An argon-filled ionization chamber was used to detect the incident intensity on the sample and a scintillation counter was used for the detection of transmitted intensity. The goniometer section of spectrometer was filled with helium buffer gas to avoid the strong air absorption of X-rays. Ten spectra were acquired and averaged for each sample.

2.5. Raman, ^{7}Li MAS NMR and EPR

Raman spectra were collected using a He–Ne laser at 632.8 nm with a laser power of about 1 mW. An incident laser spot (2 μm) was focused on the powder samples sealed in glass capillaries, under the assistance of a microscope objective. Spectra were recorded at several different sample positions. Solid state ^{7}Li magic angle spinning (MAS, with a spinning speed of 40 kHz) nuclear magnetic resonance (NMR) experiments were performed on a Bruker Advance spectrometer using 1.8 mm MAS probe at room temperature (90°/180° pulses of 2/4 μs). Spectra were referenced to a 1 M LiCl solution at 0 ppm. Electron paramagnetic resonance (EPR) spectra were recorded at room temperature with powders sealed in a 4 mm quartz tube.

3. Results and discussion

3.1. X-ray diffraction

Nanoscale isostructural Li_2VO_2F and Li_2VO_3 were synthesized by a high energy ball-milling technique using lithium oxide/fluoride and vanadium oxide as precursors in an inert atmosphere. The total scattering data were collected with synchrotron X-ray diffraction and subsequently converted to d spacing values (Fig. 2a). The XRD pattern for Li_2VO_3 resembles that for Li_2VO_2F, suggesting long-range structural similarities. Rietveld refinement confirms that both materials crystallize in the same cubic $Fm\bar{3}m$ symmetry with a DRS structure (Fig. S1†). Li and V cations (2 : 1) intermix evenly at the 4a Wyckoff sites, whereas the anion sublattice is occupied by O^{2-} for Li_2VO_3 or mixed O^{2-}/F^- for Li_2VO_2F. The interplanar spacing d_{200} is directly related to the nearest cation–anion distance (a/2) in the cubic symmetry, which shows quite close values for Li_2VO_3 and Li_2VO_2F. The lattice constant was further refined to be a = 4.1178 Å for Li_2VO_2F and a = 4.1043 Å for Li_2VO_3, respectively.

Note that the Rietveld technique is not able to account for the local distortion at the atomic scale. Hence, the atomic PDF analysis of the diffraction data, which considers both Bragg and diffuse scatterings, was performed to probe the short-range and intermediate-range structural information independent of the long-range order.

3.2. Atomic PDF analysis

The atomic PDF, $G(r)$, decays to zero at $r \approx 100$ Å for Li_2VO_2F and Li_2VO_3 (Fig. S2†), indicating a crystallite size of about 10 nm. For r-range from 1.5 to 10 Å, the experimental PDF profiles for all samples show large similarities (Fig. 2b). For Li_2VO_2F, the PDF profile can be well fitted using the average Rietveld structure model (Fig. 3a). Moreover, the local structural imperfections can be visualized directly from the PDF fitting. The local distortions are evidenced by the deviations of the first two PDF peaks (d_{4a-4b}, d_{4a-4a} or d_{4b-4b}) from the expected interatomic distances of a/2 and $a/\sqrt{2}$ (indicated with arrows in Fig. 3a) in the lattice with atoms constrained to particular positions. Such distortions reveal the difference in local bond lengths in the octahedral units. By further refining the atomic positions of F and the

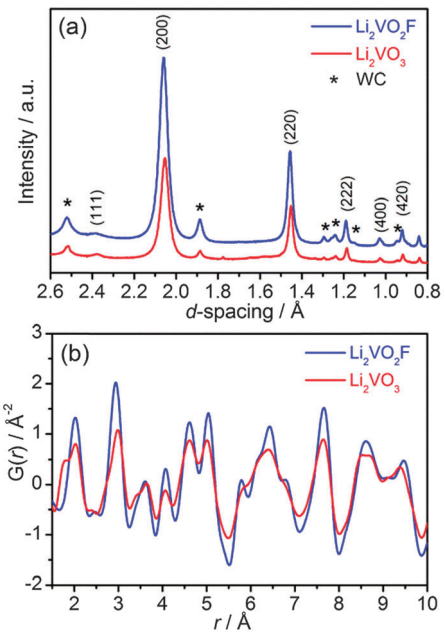

Fig. 2 (a) Synchrotron XRD patterns (λ = 0.41343 Å), and (b) atomic PDF profiles in the r-range from 1.5 to 10 Å for Li_2VO_2F and Li_2VO_3.

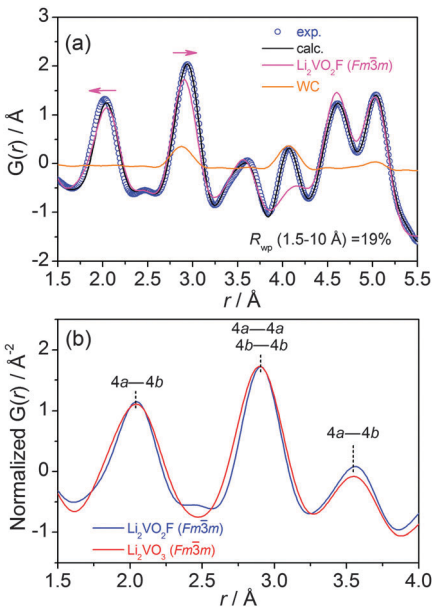

Fig. 3 (a) Experimental and calculated (using Rietveld average structure model) atomic PDF profile for Li_2VO_2F, U_{iso} (Å^2) parameters for Li, V, O and F are 0.0024, 0.0122, 0.0128 and 0.1721, respectively. (b) Modelled PDF profiles for two $Fm\bar{3}m$ phases with oxo and oxofluoro anion ligands in the r-range of 1.5–4 Å.

isotropic atomic displacement parameter ($U_{iso,F}$ = 0.028 Å^2), one can obtain an improvement in the reliability factor (R_{wp}) from 19% to 6.8%.

For Li_2VO_3, a shoulder PDF peak located at a shorter bond length (1.74 Å) was observed (Fig. 2b). The PDF profile for Li_2VO_3 cannot be successfully fitted using crystallographic structure models derived from Rietveld refinement by considering only a single $Fm\bar{3}m$ phase. Attempts to refine the structure using an assumed starting model with a NaCl superstructure ($LiVO_2$-like phase, $Fd\bar{3}m$), as previously discussed by Pralong[31] and Chieh,[32] do not yield a good fit. Instead, PDF refinement by introducing a monoclinic phase ($LiVO_3$, $C2/c$) yields an improved fit (R_{wp} = 16%) (Fig. S3†). This suggests that $LiVO_3$ exists as an amorphous component in the as-milled material, which is undetectable by synchrotron XRD. This shoulder at 1.74 Å can be assigned to the V–O bonds of the tetrahedral VO_4 structural units in the monoclinic $LiVO_3$ ($C2/c$) amorphous phase.[33] A quantification analysis from the PDF data suggests a phase fraction of 25% for the amorphous component.

The presence of the amorphous $LiVO_3$ was further checked by Raman spectroscopy. The Raman spectrum for the disordered Li_2VO_2F (O_h^5 symmetry) is nearly featureless (Fig. S4†), which arises from the random distribution of cations/anions and the fluctuation in the cation–anion bond distances. In contrast, several Raman bands at 818, 787 and 369 cm^{-1} were observed for the as-milled Li_2VO_3 (Fig. S4†). These Raman features bear a likeness to that of a high-pressure phase of amorphous $LiVO_3$ with structural deformation.[34]

The PDF corresponding to the $Fm\bar{3}m$ phase with oxo and oxofluoro anions was extracted from the raw PDF multi-phase data and plotted together with intensities normalized arbitrarily, keeping the first two peaks superimposed (Fig. S5†). It can be seen that Li_2VO_2F has slightly larger lattice dimension compared to Li_2VO_3. In Fig. 3b, PDF profiles in short range (1.5–4 Å) are shown to highlight the nearest bonding character at approximately a unit lattice dimension. The three PDF peaks correspond to the bond lengths of the nearest cation–anion (4*a*–4*b*), the nearest cation–cation (4*a*–4*a*) or anion–anion (4*b*–4*b*), and the second nearest cation–anion (4*a*–4*b*) in the cubic $Fm\bar{3}m$ structure. The V(Li)–O(F) bond distances are centered around the same values. The relative intensities of the correlations are nearly identical. In addition, the width of the PDF peak reflects the distribution of atomic distances and the correlation of atomic thermal motions. The oxyfluoride shows narrower PDF peaks than the oxide. It is deduced that the oxofluoro ligands do not cause a significant increase in the degree of distortion compared to the oxo counterpart.

3.3. ^{7}Li NMR and EPR

^{7}Li MAS NMR measurements were performed for the as-milled Li_2VO_3 in order to probe the local Li environments. A broad ^{7}Li resonance line (with a linewidth of 58 ppm) centred at −24.6 ppm was observed (Fig. S6†), together with a sharp signal at ~0 ppm (Li-containing species from diamagnetic impurities). Compared to Li_2VO_2F (−9.1 ppm),[18] the more negatively shifted ^{7}Li isotropic line for Li_2VO_3 indicates the presence of Li^+–O–V^{4+} interactions. The random cationic distribution in the DRS phase is responsible for the large distribution of chemical shifts and the broad ^{7}Li signal,[35] as also observed for Li_2VO_2F.[18] Li species in the amorphous $LiVO_3$ cannot be resolved. EPR was applied to probe the presence of V^{4+} in these samples, which can supplement NMR. Note that V^{5+} is diamagnetic and cannot exhibit EPR, whereas V^{3+} is paramagnetic and its EPR is rarely observed under ambient experimental conditions.[36] Li_2VO_3 shows a reasonably intense EPR signal (Fig. S6†), compared to Li_2VO_2F (with trace amounts of V^{4+} due to a non-stoichiometric composition).[18]

3.4. V K-Edge XANES

Further spectroscopic characterization using element-specific and oxidation state-sensitive techniques were performed to discriminate the electronic structures of V for both materials. The normalized V K-edge XANES spectra together with the first derivative spectra for the as-milled Li_2VO_2F and Li_2VO_3 are shown in Fig. 4. For comparison, the XANES spectra for several reference materials V_2O_3 (V^{3+}), V_2O_5 (V^{5+}) and VOF_3 (V^{5+}) are also shown. Similar to V_2O_3, Li_2VO_2F has a weak pre-edge absorption located at about 5.468 keV. In contrast, a more prominent pre-edge peak located at a higher energy of 5.469 keV was observed for Li_2VO_3. Pre-edge peaks can be attributed to quadrupole 1s–3d transitions or dipole transitions to the 3d states hybridized with p-states. The high intensity of the pre-edge feature in Li_2VO_3 indicates noncentrosymmetric coordination, as is found in several vanadium oxides.[37] Both Li_2VO_2F and Li_2VO_3 show strong whiteline peaks, compared to the reference materials. The main absorption edge (dipole-allowed 1s–4p transition) for Li_2VO_3 is located at higher energy (an energy shift by ~2 eV) than that for Li_2VO_2F, indicating a higher average oxidation state of V. In addition, the main absorption edge shapes for Li_2VO_2F and Li_2VO_3 are very similar with shoulder peaks at 5.475 keV (1s–4p shakedown transition). Such absorption features can be better seen in the derivative spectra. The local coordination symmetries of V absorbers in Li_2VO_2F and Li_2VO_3 will be further studied by extended X-ray absorption fine structure using synchrotron radiation in future.

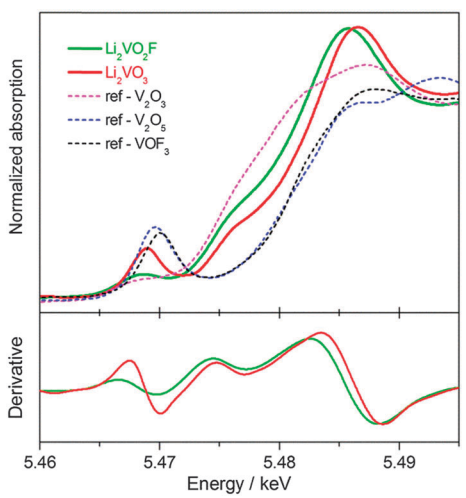

Fig. 4 V K-edge XANES spectra and the derivative plots for Li_2VO_2F and Li_2VO_3.

3.5. Galvanostatic electrochemical cycling

The above-mentioned analysis confirms the structural similarity between the Li_2VO_3 and Li_2VO_2F, which makes these materials ideally suitable for a comparative study of the anion chemistry in electrochemical intercalation reactions. For Li_2VO_3, only the V^{4+}/V^{5+} redox couple is active for lithium storage. In contrast, Li_2VO_2F has a high theoretical capacity of 462 mA h g^{-1}, assuming a two-electron V^{3+}/V^{5+} oxidation reaction. The charge–discharge performance for Li_2VO_3 and Li_2VO_2F was compared between 4.1 and 1.3 V at 25 °C and at a rate of C/20 based on their theoretical capacities. The distinct voltage profiles for the first two cycles are shown in Fig. 5a. The charge–discharge capacity was calculated based on the mass of corresponding active materials. Li_2VO_2F delivers a capacity of 330 mA h g^{-1} (exchange of about 1.4Li^+) at 25 °C. Up to 1.8Li^+ exchange has been previously observed at elevated temperature and at low current rate.[18] For Li_2VO_3, a capacity of about 295 mA h g^{-1} was observed, indicating a possible large contribution from amorphous $LiVO_3$.[38] Above 3.7 V, the charge curve for Li_2VO_3 shows a fast increase in voltage compared to that for Li_2VO_2F. Note that a full capacity for a $Fd\bar{3}m$ $Li_{2-x}VO_3$ and a $C2/c$ $LiVO_3$ has been reached when cycling between 3.5 and 1 V.[31,38] Thus, the overcharge of Li_2VO_3 to 4.1 V may trigger the electrolyte decomposition. The second charge curves for both materials are roughly overlapped. However, the discharge curves shift down by about 0.3 V for Li_2VO_3 compared to that for Li_2VO_2F. The onset discharge voltage is about 3.5 V for Li_2VO_3, which is lower than that of about 4 V for Li_2VO_2F. The average discharge voltage is about 2.2 V for Li_2VO_3 and about 2.5 V for Li_2VO_2F. The higher lithiation voltage for the oxyfluoride is believed to be related to the presence of the F ligand with high electronegativity. The sloping profiles suggest a single-phase intercalation mechanism for both materials.

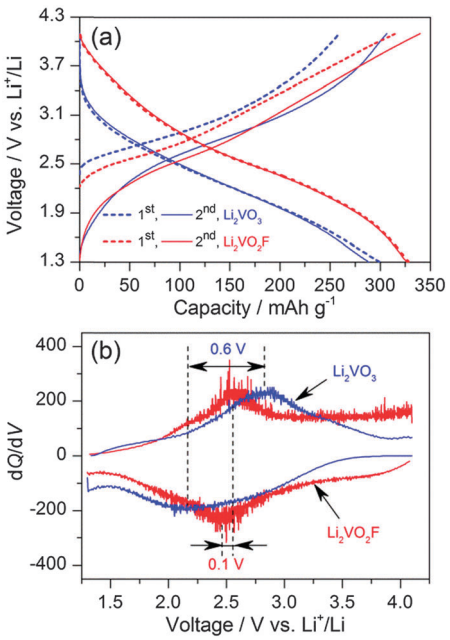

Fig. 5 (a) Voltage profiles for Li_2VO_3 and Li_2VO_2F measured between 1.3 and 4.1 V. (b) dQ/dV plots from the second cycles.

The dQ/dV curves in Fig. 5b show the difference in the centred redox voltages, which is about 0.6 V for Li_2VO_3 in comparison with only 0.1 V for Li_2VO_2F. Bearing in mind the above observations, it is remarkable that Li_2VO_2F allows about 1.4Li^+ intercalation reaction (a dominate $V^{4.4+}/V^{3+}$ reduction) centred at ~2.5 V with oxofluoro ligands, in contrast to the 1.0Li^+ intercalation process (V^{5+}/V^{4+} reduction) at ~2.2 V for Li_2VO_3 with oxo ligands. Low onset discharge voltage (~3.5 V), low average discharge voltage (~2.3 V) and large voltage hysteresis (~0.7 V) were also found in other vanadium-based DRS materials with oxo ligands.[24] These observations suggest that the ligand anions play a predominate role in the electrochemical properties in terms of energy density and energy efficiency.

3.6. EIS Studies

EIS spectra were recorded to extract the characteristic kinetic parameters such as the charge transfer resistance (R_{ct}) and the Li^+ chemical diffusion coefficients (D_{Li^+}) for Li_2VO_3 and Li_2VO_2F. All the Nyquist plots consist of two depressed semicircles at high and middle frequency regions and an inclined straight line at the low frequency region (Fig. 6). The R_{ct}, which defines the transport rate of charge carriers across the electrode/electrolyte interface, is estimated from the EIS fitting (χ^2 ranging from 10^{-4} to 10^{-6}) of the high and middle frequency semicircle regions (3 Hz–10 kHz for Li_2VO_3, and 10 Hz–10 kHz for Li_2VO_2F) using a proposed equivalent circuit by Levi *et al.*,[39] consisting of the solution resistance and two parallel RQ elements in series.

Fig. 7a shows the variation of R_{ct} at different voltages. Li_2VO_2F showed lower R_{ct} compared to Li_2VO_3, indicating fast kinetics of the electrode reaction. This provides physical interpretation of the electrochemical polarization behaviour for both materials. In addition, for Li_2VO_2F, R_{ct} showed a relatively small variation with voltage (*i.e.*, Li content), compared to that for Li_2VO_3. These observations suggest that the microscopic Li^+ diffusion behaviour can be largely

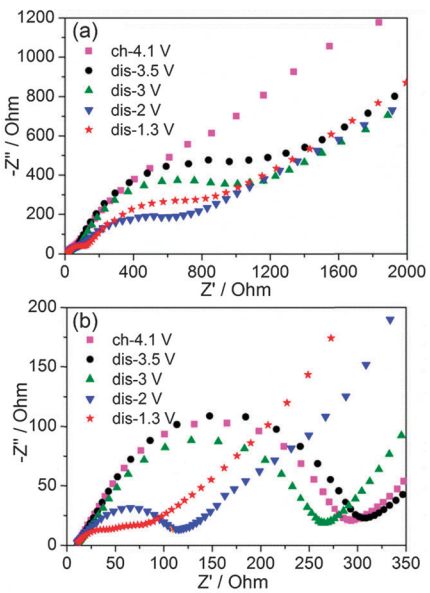

Fig. 6 Nyquist plots of (a) Li_2VO_3 and (b) Li_2VO_2F at various voltages.

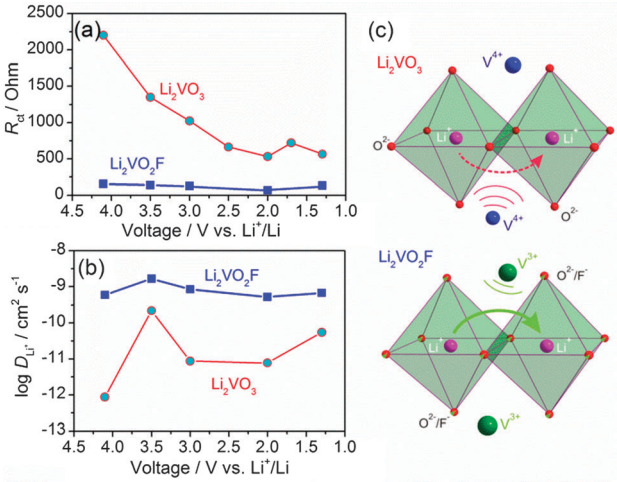

Fig. 7 Variation of (a) R_{ct} and (b) D_{Li^+} at different voltages for Li_2VO_3 and Li_2VO_2F. (c) Schematic view of the Li^+ migration through the o–t–o path indicated by curved arrows, which is subjected to the electrostatic repulsion from neighbouring vanadium cations in the lattice. Note that Li (purple spheres) and V (blue/green spheres) have a statistical distribution of 2 : 1 at the cationic sites. Anions O^{2-} and O^{2-}/F^- are represented by small red and red/green spheres, respectively.

different due to the difference in atomic configuration of the rocksalt structural units although the dilithium composition in DRS assures a macroscopic percolating network for Li^+ migration.[26]

3.7. Li^+ Diffusivity

The diffusion-controlled Warburg impedance and its dependence on lithium content for Li_2VO_3 and Li_2VO_2F were studied by analysing the low frequency complex impedance regions. The D_{Li^+} at different voltages were calculated according to the equation: $D_{Li^+} = 1/2(V_m/SF\sigma)^2(dE/dx)^2$,[40] where V_m is the molar volume, S is the contact area between electrolyte and sample, F is the Faraday constant, σ is the Warburg coefficient and dE/dx is the slope of open-circuit voltage *versus* Li^+ concentration. The Warburg coefficient (σ) can be determined from the slope of the real resistance (Z') *versus* the inverse square root of the angular frequency ($\omega^{-0.5}$) of the low-frequency impedance data (Fig. S7†). A linear behaviour was observed for frequency between 10 and 1 mHz. D_{Li^+} as a function of lithium content for the materials is shown in Fig. 7b. The experimentally estimated D_{Li^+} is about 10^{-9} cm^2 s^{-1} for Li_2VO_2F, which is about two orders of magnitude higher than that for Li_2VO_3 (10^{-11} cm^2 s^{-1}). Considering that a high D_{Li^+} ($\sim 10^{-9}$ cm^2 s^{-1}) has been reported for a $C2/c$ $LiVO_3$ for lithium intercalation,[38] the presence of the amorphous $LiVO_3$ in the material should not affect largely the apparent EIS behaviour of Li_2VO_3. Hence, these results indicate that the Li^+ migration is relatively facile for Li_2VO_2F. These transport properties correlate directly to their distinct kinetic behaviour.

It is assumed that an unimpeded Li^+ diffusion pathway is maintained for $Li_{2-x}VO_2F$ with the variation of x upon cycling, arising from the free Li^+ transport manner in a DRS structure. This is in contrast to the increase in the Li^+ diffusion barrier for layered structure with a progressive narrowing of the Li-slab distance during Li^+ removal.[41] For layered rocksalt $LiVO_2$, cation migration from original octahedral sites to tetrahedral sites has been observed upon partial Li^+ removal.[42] However, so far no evidence has been found for such cation migration in Li_2VO_2F.[18] Further work is on-going to clarify the local structural features of the materials upon Li^+ removal in the DRS structure.

On the basis of the *ab initio* computations by Ceder *et al.*,[19,26] it is anticipated that Li^+ hopping from one octahedral site to its neighbouring octahedral site through a vacant interstitial tetrahedral site (*i.e.*, o–t–o diffusion path, as denoted by the arrows in Fig. 7c) can proceed with large freedom for Li_2VO_2F and Li_2VO_3 with high overall Li^+ concentration (2/3 of the cationic sites are occupied by Li^+). The dilithium chemical composition with DRS structure ensures the percolation diffusion channel spanning the entire structure. The Li^+ migration through the tetrahedral site, which shares face with the octahedral V cation, will be subjected to the electrostatic repulsion from the neighbouring V cation. Earlier *ab initio* computations on layered materials showed that the high-valent cation will have a negative impact on the activation energy for Li^+ transport.[43–45] It is a straightforward case that the electrostatic repulsion between the mobile Li^+ and its neighbouring V^{4+} in Li_2VO_3 is higher than that between Li^+ and V^{3+} in Li_2VO_2F (Fig. 7c). Li^+ hopping through an o–t–o path in Li_2VO_2F is energetically more favourable than that in Li_2VO_3. Thus, in spite of the extremely high crystallographic similarities between Li_2VO_3 and Li_2VO_2F, the different anionic environment and the difference in the valence of vanadium lead not only to a different redox energy of vanadium, but also to a significant impact on the Li^+ hopping behaviour in the lattice. In general, the size difference of anions can alter the dimension of the unit cell and affect the Li^+ diffusivity.[45] Additionally, anions with different electron charge densities and their local spatial distributions in the crystal structures can contribute to considerable differences in the activation barrier. These issues need to be addressed in future work. Divergences in the bonding character, atomic charges, electron density and electrostatic interaction across two isostructural samples with a DRS structure illustrate how material properties can vary largely depending on the anion environment.

4. Conclusions

In summary, we correlated the chemical/electronic nature to the electrochemical/kinetic behaviour of intercalation materials Li_2VO_3 and Li_2VO_2F with an isostructural DRS structure. Detailed crystallographic and spectroscopic characterizations were performed to identify the structure of the studied materials. Besides the higher theoretical and practical capacity of the oxyfluoride (Li_2VO_2F), improved electrochemical performance (higher voltage, lower polarization and better Li^+ diffusivity) was also observed over its oxide analogue (Li_2VO_3). These comparative studies demonstrate how to enhance cathode performance by simply

controlling the anion chemistry through incorporating a high electronegativity anion ligand into the crystal structure. In addition, our further work has also proven that even higher voltage and accordingly higher energy density can be achieved in such an oxyfluoride system.[46] The combination of DRS structure and mixed anion chemistry would be of general interest for designing new high-performance energy storage materials.

Acknowledgements

We acknowledge the allocated synchrotron beamtime at the ALBA Synchrotron Light Source, Spain. We thank I. Peral for fruitful PDF discussions and S. Lebedkin for assisting the Raman measurements. A.G. would like to thank support from Russian Ministry of Education and Science (MK-3206.2014.2). R.W. thanks the EU Fund, Estonian Research Council, TUT and KBFI (MTT68, SF0690034s09, B618 and PUT126).

Notes and references

1 M. S. Whittingham, *Chem. Rev.*, 2004, **104**, 4271.
2 J. B. Goodenough and Y. Kim, *Chem. Mater.*, 2010, **22**, 587.
3 P. Poizot, S. Laruelle, S. Grugeon, L. Dupont and J.-M. Tarascon, *Nature*, 2000, **407**, 496.
4 K. Mizushima, P. C. Jones, P. J. Wiseman and J. B. Goodenough, *Mater. Res. Bull.*, 1980, **15**, 783.
5 T. Ohzuku and Y. Makimura, *Chem. Lett.*, 2001, 642.
6 M. M. Thackeray, P. J. Johnson, L. A. de Picciotto, P. G. Bruce and J. B. Goodenough, *Mater. Res. Bull.*, 1984, **19**, 179.
7 R. Chen, M. Knapp, M. Yavuz, R. Heinzmann, D. Wang, S. Ren, V. Trouillet, S. Lebedkin, S. Doyle, H. Hahn, H. Ehrenberg and S. Indris, *J. Phys. Chem. C*, 2014, **118**, 12608.
8 B. C. Melot and J.-M. Tarascon, *Acc. Chem. Res.*, 2013, **46**, 1226.
9 A. S. Aricò, P. Bruce, B. Scrosati, J.-M. Tarascon and W. Van Schalkwijk, *Nature Mater.*, 2005, **4**, 366.
10 N. Recham, J.-N. Chotard, L. Dupont, C. Delacourt, W. Walker, M. Armand and J.-M. Tarascon, *Nature Mater.*, 2010, **9**, 68.
11 N. Pereira, F. Badway, M. Wartelsky, S. Gunn and G. G. Amatucci, *J. Electrochem. Soc.*, 2009, **156**, A407.
12 M. Leblanc, V. Maisonneuve and A. Tressaud, *Chem. Rev.*, 2015, **115**, 1191.
13 D. Dambournet, K. W. Chapman, P. J. Chupas, R. E. Gerald II, N. Penin, C. Labrugere, A. Demourgues, A. Tressaud and K. Amine, *J. Am. Chem. Soc.*, 2011, **133**, 13240.
14 M. Duttine, D. Dambournet, N. Penin, D. Carlier, L. Bourgeois, A. Wattiaux, K. W. Chapman, P. J. Chupas, H. Groult, E. Durand and A. Demourgues, *Chem. Mater.*, 2014, **26**, 4190.
15 G. Hautier, A. Jain, H. Chen, C. Moore, S. P. Ong and G. Ceder, *J. Mater. Chem.*, 2011, **21**, 17147.
16 K. M. Wiaderek, O. J. Borkiewicz, E. Castillo-Martínez, R. Robert, N. Pereira, G. G. Amatucci, C. P. Grey, P. J. Chupas and K. W. Chapman, *J. Am. Chem. Soc.*, 2013, **135**, 4070.
17 N. A. Chernova, M. Roppolo, A. C. Dillon and M. S. Whittingham, *J. Mater. Chem.*, 2009, **19**, 2526.
18 R. Chen, S. Ren, M. Knapp, D. Wang, R. Witter, M. Fichtner and H. Hahn, *Adv. Energy Mater.*, 2015, **5**, 1401814; R. Chen, S. Ren, S. Indris, M. Fichtner and H. Hahn, *European Pat.*, EP 14160894.3, 2014.
19 J. Lee, A. Urban, X. Li, D. Su, G. Hautier and G. Ceder, *Science*, 2014, **343**, 519.
20 N. Yabuuchi, M. Takeuchi, D. Endo, T. Ozaki, T. Inamasu, J.-Y. Son, Y.-T. Cui, H. Oji and S. Komaba, 224th ECS Meeting (The Electrochemical Society, 2013).
21 L. Zhang, H. Noguchi, D. Li, T. Muta, X. Wang, M. Yoshio and I. Taniguchi, *J. Power Sources*, 2008, **185**, 534.
22 M. Küzma, R. Dominko, A. Meden, D. Makovec, M. Bele, J. Jamnik and M. Gaberšček, *J. Power Sources*, 2009, **189**, 81.
23 M. Yang, X. Zhao, Y. Bian, L. Ma, Y. Ding and X. Shen, *J. Mater. Chem.*, 2012, **22**, 6200.
24 R. Dominko, C. Vidal-Abraca Garrido, M. Bele, M. Kuezma, I. Arcon and M. Gaberscek, *J. Power Sources*, 2011, **196**, 6856.
25 M. N. Obrovac, O. Mao and J. R. Dahn, *Solid State Ionics*, 1998, **112**, 9.
26 A. Urban, J. Lee and G. Ceder, *Adv. Energy Mater.*, 2014, **4**, 1400478.
27 J. Rodríguez-Carvajal, *Physica B*, 1993, **192**, 55.
28 A. P. Hammersley, S. O. Svenson, M. Hanfland and D. Hauserman, *High Pressure Res.*, 1996, **14**, 235.
29 P. Juhás, T. Davis, C. L. Farrow and S. J. L. Billinge, *J. Appl. Crystallogr.*, 2013, **46**, 560.
30 Th. Proffen and S. J. L. Billinge, *J. Appl. Crystallogr.*, 1999, **32**, 572.
31 V. Pralong, V. Gopal, V. Caignaert, V. Duffort and B. Raveau, *Chem. Mater.*, 2012, **24**, 12.
32 C. Chieh, B. L. Chamberland and A. F. Wells, *Acta Crystallogr. B*, 1981, **37**, 1813.
33 S. Hayakawa, T. Yoko and S. Sakka, *J. Solid State Chem.*, 1994, **112**, 329.
34 A. Grzechnik and P. F. McMillan, *J. Phys. Chem. Solids*, 1995, **56**, 159.
35 R. Chen, M. Knapp, M. Yavuz, S. Ren, R. Witte, R. Heinzmann, H. Hahn, H. Ehrenberg and S. Indris, *Phys. Chem. Chem. Phys.*, 2015, **17**, 1482.
36 C. P. Poole and H. A. Farach, *The Theory of Magnetic Resonance*, Wiley-Interscience, New York, 1972.
37 J. Wong, F. W. Lytle, R. P. Messmer and D. H. Maylotte, *Phys. Rev. B*, 1984, **30**, 5596.
38 X. M. Jian, J. P. Tu, Y. Q. Qiao, Y. Lu, X. L. Wang and C. D. Gu, *J. Power Sources*, 2013, **236**, 33.
39 M. D. Levi, K. Gamolsky, D. Aurbach, U. Heider and R. Oesten, *Electrochim. Acta*, 2000, **45**, 1781.
40 C. Ho, I. D. Raistrick and R. A. Huggins, *J. Electrochem. Soc.*, 1980, **127**, 343.

41 A. Van der Ven, J. Bhattacharya and A. A. Belak, *Acc. Chem. Res.*, 2013, **46**, 1216.
42 M. M. Thackeray, L. A. de Picciotto, W. I. F. David, P. G. Bruce and J. B. Goodenough, *J. Solid State Chem.*, 1987, **67**, 285.
43 K. Kang, Y. S. Meng, J. Bréger, C. P. Grey and G. Ceder, *Science*, 2006, **311**, 977.
44 A. Van der Ven and G. Ceder, *J. Power Sources*, 2001, **97–98**, 529.
45 K. Kang and G. Ceder, *Phys. Rev. B*, 2006, **74**, 094105.
46 S. Ren, R. Chen, E. Maawad, O. Dolotko, A. A. Guda, V. Shapovalov, D. Wang, H. Hahn and M. Fichtner, *Adv. Sci.*, 2015, DOI: 10.1002/advs.201500128.